

A technique for diagnosing moisture dynamics in GCMs

Joseph Galewsky ^{*}and Adam Sobel

Department of Applied Physics and Applied Mathematics

Columbia University

New York, NY

Isaac Held

Geophysical Fluid Dynamics Laboratory/NOAA

Princeton University

Princeton, NJ

April 5, 2004

^{*}Corresponding author: Email jg2282@columbia.edu

Abstract

A technique for diagnosing mechanisms controlling the water vapor distribution in a general circulation model (GCM) is presented. The technique involves defining a large number of tracers, each of which represents air which has last been saturated in a particular region of the atmosphere. The time-mean, zonal-mean tracer fields show the typical pathways that air parcels take between one occurrence of saturation and the next. Because saturation vapor pressure is a function only of temperature, and because mixing ratio is conserved for unsaturated parcels, these tracer fields can be used together with the temperature field to reconstruct the water vapor field. This method clarifies the separate influences of temperature and circulation on the water vapor field.

The technique is applied to an idealized GCM in which the dynamics are dry and forced using the Held-Suarez thermal relaxation, but the model carries a passive water-like tracer which is emitted at the surface and lost due to large-scale condensation with zero latent heat release and no condensate retained. The technique provides an accurate reconstruction of the simulated water vapor field. In this model, the dry air in the subtropical troposphere is produced primarily by isentropic transport, and is moistened somewhat by mixing with air from lower levels which has not been saturated since last contact with the surface. The authors suggest that the technique could be potentially useful in assessing the roles of temperature, circulation, and cloud microphysics in the maintenance of relative humidity in comprehensive GCMs.

1 Introduction

The water vapor distribution in the atmosphere is influenced by several different processes: surface evaporation, transport by fluid motion, convection, and cloud microphysics. The latter two processes, in particular present difficult challenges to climate models. Though all these processes play some role in the maintenance of the atmospheric water vapor distribution, the relative importance of each is subject to debate.

Several studies (Sherwood, 1996; Salathe and Hartmann, 1997; Pierrehumbert and Roca, 1998; Dessler and Sherwood, 2000) have shown that the observed humidity distribution in the troposphere can, to first order, be reconstructed by considering the large-scale circulation as given and using it to advect a passive water-like tracer, without any explicit parameterization of convection or cloud microphysics (though information about convective heating is implicit in the circulation itself). The tracer is assumed to condense at the dewpoint (T_d), though no latent heat is released.

In this simplified picture, we assume that upward motion leads to saturation, and that all condensate rains out immediately. Once air parcels begin descending and warming in downward branches of the circulation, they conserve water vapor mixing ratio until they either ascend and saturate again, or come in contact with the surface where water vapor is emitted. Up to that point, we can think of the mixing ratio of each parcel as being set by the saturation vapor pressure at the temperature at which it was last saturated. Of course, mixing occurs, so that in reality an air parcel's mixing ratio represents an average over a spectrum of last saturation temperatures determined by the paths of the different “sub-parcels” which constitute the parcel.

Even in this picture, there is some complexity. In a climate change, we expect that both

the temperature field and the circulation may change, in general. Both changes can affect the humidity field, as we can see by imagining changes in one absent changes in the other (ignoring for the sake of argument the fact that the two are dynamically related). If the circulation were constant, the temperature of last saturation of air parcels would change because of the temperature change. If the circulation were to change in the absence of a temperature change, the temperature of last saturation of parcels could change, as well as the paths taken after last saturation.

We present a technique for diagnosing the roles of temperature and circulation in determining the water vapor distribution. The technique is closely related to Green's function or boundary propagator methods (Hall and Plumb, 1994; Holzer and Hall, 2000; Haine and Hall, 2002) as well as, somewhat less directly, the transilient matrix approach (Stull, 1984; Ebert et al., 1989; Stull, 1993; Sobel, 1999; Larson, 1999), all of which have been applied in different contexts. We apply our technique to an idealized atmospheric general circulation model (GCM) based on the simple picture described above, focusing on the relative humidity of the troposphere. Dynamically, our GCM is a dry model, thermally forced by relaxation to a prescribed equilibrium state (Held and Suarez, 1994). It carries a passive water vapor-like tracer, which condenses according to the Clausius-Clapeyron relation obeyed by real water vapor, but whose latent heat of vaporization is set to zero, so that it does not influence the flow. This model is useful for testing our diagnostic technique since any errors which occur can be unambiguously assigned to the discretization and averaging which the technique employs, rather than to cloud microphysics or other subgrid-scale processes which our model does not contain. If we can understand and control these inherent errors, we can then go on to apply the technique to more comprehensive atmospheric models. In such models, by quantifying the roles of temperature and circulation using the present method, we may also

hope to clarify the role of microphysics in determining the water vapor distribution.

2 Numerical Model Configuration

2.1 AGCM setup

We use the dynamical core of the Flexible Modeling System (FMS) developed at the Geophysical Fluid Dynamics Lab. Our model solves the hydrostatic primitive equations in sigma coordinates (20 equally spaced vertical levels) and uses the spectral transform method in the horizontal, Simmons and Burridge (1981) finite differencing in the vertical, and an Asselin-filtered semi-implicit leapfrog scheme for time integration. The results presented here were computed at a T42 spectral resolution, though similar results were obtained for a T85 model.

The model is forced by Newtonian relaxation of the temperature toward a prescribed, zonally symmetric, equilibrium temperature (Held and Suarez, 1994) of the form

$$T_{\text{eq}} = \max \left\{ T_{\text{st}}, \left[(T_0 - \Delta H \sin^2(\phi)) - \Delta_V \cos^2(\phi) \log \left(\frac{p}{p_0} \right) \right] \left(\frac{p}{p_0} \right)^\kappa \right\} \quad (1)$$

where ϕ is the latitude, T_{st} is the stratospheric temperature, T_0 is the equilibrium temperature at the surface at the equator, Δ_H is the horizontal equator-to-pole temperature gradient, and ΔH controls the static stability. The values used in this study are (in Kelvin degrees): $T_{\text{st}} = 200$, $T_0 = 315$, $\Delta H = 60$, $\Delta V = 10$.

Planetary boundary-layer drag is represented by Rayleigh damping. The frictional damping at the surface is -1.0 d^{-1} and decays linearly to the top of the planetary boundary layer at $\sigma = 0.7$. All of the results here are 2800 day averages taken from a 3000 day run, with the first 200 days of integration discarded.

The tracer advection algorithm is a piecewise parabolic scheme in the vertical (Colella

and Woodward, 1984) and piecewise linear in the horizontal (van Leer, 1979). Since the spectral model uses the log of the surface pressure as a prognostic variable, tracer mass cannot be conserved exactly. Instead, we use the advective form of the tracer equation in the faux flux form

$$v \cdot \nabla \xi = \nabla \cdot (v \xi) - \xi \nabla \cdot v \quad (2)$$

treating the first term on the RHS on the sphere following Lin and Rood (1996) and the second term in such a way that a uniform tracer remains exactly uniform. Exact conservation is not of central importance for a tracer with a short lifetime, such as tropospheric water.

We consider the large-scale advection and condensation of a passive water vapor tracer; no latent heat is released upon condensation and there is no convective parameterization in the model. Water vapor is introduced into the lowest 50 hPa at a fixed rate according to the following function:

$$r_0(\phi, 0, t) = \frac{f_m g \cos(\phi)^2}{\Delta P} \quad (3)$$

where r_0 is the mixing ratio in the lowest model level, ϕ is the latitude f_m is the moisture flux, g is the acceleration due to gravity (9.8 m/s^2), and ΔP is the change in pressure across the source layer. This function has a maximum at the equator and decays to zero at the poles. For the results presented here, $f_m = 2.3 \times 10^{-5} \frac{\text{kg}}{\text{m}^2 \text{s}}$ and $\Delta P = 50 \text{ hPa}$, which corresponds to a maximum moisture flux of about 2.5 mm/day. At each time step, the relative humidity (RH) is calculated in each cell. If that cell is saturated, the excess moisture is removed and is assumed to rain out immediately. No condensate is carried in the model. This simple passive water vapor calculation, coupled to the Held-Suarez-type forcing as described here, may be a useful benchmark for testing advection algorithms.

2.2 Tracer Calculation

We now describe the technique we have developed to separate the influences of temperature and circulation on the humidity field. We divide the global model domain into N axisymmetric subdomains, \mathcal{D}_i , where i is an index ranging from 1 to N . In the particular implementation shown here, each domain spans $\pi/8$ radians of latitude and 2 vertical levels (100 hPa). Each subdomain \mathcal{D}_i is assigned a tracer, \mathcal{T}_i . Each grid cell in the model domain is thereby associated with a subdomain and a tracer. All the tracers are defined over the entire global domain, but are associated with their subdomains in the following way.

Consider a saturated grid cell with latitude ϕ altitude z , and longitude λ . This cell resides in one of the N subdomains, \mathcal{D}_s , and is therefore associated with a tracer \mathcal{T}_s . Upon saturation in that cell, we set \mathcal{T}_s to unity,

$$\mathcal{T}_s(\phi, p, \lambda) = 1, \quad (4)$$

and we set all the remaining (N-1) tracers to zero,

$$\mathcal{T}_j(\phi, p, \lambda) = 0, \quad (5)$$

where j takes on all values from 1 to N except s . Apart from the above operation, which is performed any time saturation occurs in the model, and apart from a special treatment of the lowest model level (described below), all the tracers are advected by the flow and undergo explicit and numerical diffusion.

If a particular tracer's value is exactly 1, it means that all of the air in that cell was last saturated in the subdomain associated with the tracer. In general, because of diffusion, a cell contains a mix of air last saturated in several different subdomains, so that any individual tracer value is usually less than 1. The contribution of an individual subdomain's tracer to a

particular cell can be interpreted as a probability that the air in that cell was last saturated in the subdomain. If a state were to be reached in which all of the air in a given cell had been saturated at least once, the tracers would sum to unity

$$\sum_{i=1}^N \mathcal{T}_i = 1 \quad (6)$$

in that cell. This is approximately true at upper levels (see Fig. 8c), but not necessarily close to the surface, where fresh water vapor has recently been emitted. We define a special tracer, referred to here as the source tracer, to handle this. At each time step, the source tracer is set equal to the water vapor mixing ratio at all points in the lowest level, and all of the other tracers are set to zero in the lowest level:

$$\begin{aligned} \mathcal{S}(\phi, 0, \lambda) &= r(\phi, 0, \lambda) \\ \mathcal{T}_i(\phi, 0, \lambda) &= 0 \end{aligned} \quad (7)$$

for all i, ϕ, λ , where \mathcal{S} is the source term and r is the water vapor mixing ratio. When air is saturated at any point outside the lowest model level, the source tracer at that location is set to zero.

The tracers indicate the transport pathways taken by air parcels between one instance of saturation and the next. They are designed so that they can be used, together with the saturation mixing ratios determined by the temperature field in the respective subdomains, to reconstruct the water vapor field. In the limit of infinite resolution in the subdomains ($N \rightarrow \infty$), or equivalently if the saturation mixing ratio were uniform in each subdomain, and if the circulation were purely axisymmetric and steady, we would have, exactly:

$$r(\phi, p) = \int \int \mathcal{T}(\phi, p | \phi', p') r^*(\phi', p') d\phi' dp' + \mathcal{S}(\phi, p), \quad (8)$$

where now there is a tracer $\mathcal{T}(\phi, p | \phi', p')$ for every spatial point (ϕ, p) at which saturation

may have occurred. In discrete form, with again i indexing the locations of last saturation, (8) becomes

$$r(\phi, p) = \sum_{i=1}^N \mathcal{T}_i(\phi, p) r_i^* + \mathcal{S}(\phi, p), \quad (9)$$

where r_i^* denotes the saturation mixing ratio in box i . Within each term in the sum (which dominates \mathcal{S} above the near-surface levels), the two terms in the product, the tracer and the saturation mixing ratio, encapsulate the roles of circulation and temperature, respectively. r_i^* is a function of the temperature and pressure in subdomain i , but under earthlike conditions we are safe in assuming that the temperature dependence dominates variations in r_i^* . If we can use (9) to accurately reconstruct the water vapor field both before and after a climate change, we can then examine the changes in the \mathcal{T}_i 's and r_i^* 's separately to understand the relative contributions of structures in the circulation and temperature fields to the humidity field.

In practice, we do not have an axisymmetric, steady circulation (though it is statistically axisymmetric) so we replace all fields in the above by zonal and time means. This introduces errors, because it implies an assumption that air parcels which experienced last saturation at some given location (ϕ, p, x, t) was imprinted at that time with the zonal and time mean saturation mixing ratio at (ϕ, p) . In reality, there are temporal and zonal temperature variations, so that the saturation mixing ratio may have been different from the zonal and time mean value. It is straightforward to show that if these temperature variations are correlated (positively or negatively) with variations in the probability of saturation, rectified errors occur which render (9) no longer exact.

Perhaps more importantly, the subdomain size is finite. Since each tracer requires a sep-

arate advection-diffusion calculation, computational expense increases rapidly as subdomain size decreases, and in practice we must use subdomains sufficiently large that the saturation mixing ratio varies considerably within each subdomain. The most naive approach would be to use the average saturation mixing ratio over the box in the place of r_i^* , above. In fact we can do somewhat better than this. We break the tracer fields into two components, a “local” component, $\hat{\mathcal{T}}$, and a “nonlocal” component (Fig. 1). The local component refers to the tracer within its own subdomain. Typically, when a given tracer has a significantly nonzero value in its own subdomain, that is because the air is either saturated at the moment, or has been saturated very recently; this tends to happen in subdomains located in ascending branches of the general circulation. In this situation, we can use the fact that we know the distribution of saturation mixing ratio within the subdomain, and use the local value at the grid cell in question, rather than the average over the subdomain, in the reconstruction of the humidity field. The nonlocal tracer component refers to the tracer everywhere outside of its own subdomain. In this case, all we know is that last saturation occurred somewhere within that tracer’s subdomain; we do not know at what point within the subdomain it occurred. Therefore, for the local tracer we must use the average saturation mixing ratio from the subdomain. Thus, our finite-resolution formulation for reconstructing the water vapor distribution from the tracers and the saturation mixing ratio field is:

$$r_e(\phi, p) = \sum_i \hat{\mathcal{T}}_i(\phi, p) r_i^*(\phi, p) + \sum_i \check{\mathcal{T}}_i(\phi, p) \langle r_i^* \rangle + \mathcal{S} \quad (10)$$

where r_e is the reconstructed mixing ratio, r^* is the saturation mixing ratio, $\langle r_i^* \rangle$ is the density-weighted mean of the saturation mixing ratio within the i th subdomain, and where now all fields should be read as zonal and time means. This formulation gives considerably more accurate results than does simply replacing r_i^* by $\langle r_i^* \rangle$ at all points in (9).

Because we are focusing on the troposphere, we do not actually cover the entire model atmosphere with subdomains defining associated tracers, but rather omit the top 4 levels, defining subdomains covering the region below 200 hPa. The tropopause is largely, though not entirely, a transport barrier, separating air masses of different properties. If we define subdomains straddling the tropopause, particularly in the tropics and subtropics, air descending from just below the tropopause will carry the average saturation mixing ratio of the box, which contains both stratospheric and tropospheric air. The average can be particularly unrepresentative of the actual (tropospheric) saturation mixing ratio that the parcel saw at last saturation. We have found that this can lead to large errors. Omitting the tracers associated with the top subdomains from the humidity reconstruction also induces an error, but it is a smaller one, in general, throughout the tropospheric levels below 200 hPa. If we were interested in looking closely at the levels around the tropopause, we could do so by increasing the resolution of the tracers (decreasing the box size) or, potentially, by incorporating a distinction between tropospheric and stratospheric air into the computation in some other way.

3 Results

3.1 Moisture fields

We first describe some of the time-mean, zonal-mean fields produced by the idealized GCM. In the RH field (Fig. 2a), a very humid ($\text{RH} > 90\%$) narrow equatorial zone is bounded by very dry air ($\text{RH} < 40\%$) out to about 40° latitude. The extratropics are intermediate, with relative humidities generally around $60\% - 80\%$. The RH declines very rapidly above the

tropopause, with values well below 20%.

The mixing ratio (displayed in 2b as $\log_{10}(r)$) is characterized by a moist equatorial plume with a sharp drop between the deep Tropics and the subtropics (at around 10° latitude). In general, the mixing ratio in the subtropical midtroposphere is also depressed relative to the extratropics at the same levels.

The streamfunction (Fig. 2c) for the zonal mean meridional circulation shows the expected form, including Hadley and Ferrell cells. As expected, the regions of very low RH correspond to regions of downward motion in the overturning circulation.

The potential temperature field (Fig. 2d) is broadly consistent with that observed, with the 315° isentrope connecting the tropical middle troposphere with the midlatitude upper troposphere.

The overall water vapor distribution produced by this simple model is qualitatively realistic, with a moist equatorial zone bounded by a very dry subtropical region coincident with the downward limb of the meridional overturning circulation, though the extratropics are rather more humid than observed in the real atmosphere (Peixoto and Oort, 1992).

3.2 Physical interpretation of the tracer fields

Figure 3 shows the time-mean, zonal-mean of the 28 tracer fields obtained from the idealized GCM. These fields indicate the transport pathways that air parcels take between one instance of saturation and the next. Some tracers have significant nonzero values outside of their associated subdomains, while others do not. In most of the tracer fields, the location of the associated subdomain is easily seen as a concentrated, well-defined zone of relatively large tracer value.

In the equatorial tracer fields, virtually the entire zone outside of the subdomain is zero. The tracer fields from the upper subtropical troposphere, in contrast, have prominent sloping plumes of nonzero values that descend almost to the surface, while the tracers from the lower subtropical troposphere have very low values everywhere. The extratropical tracers generally have large values within their respective subdomains and also exhibit some of the sloping plume-like structure seen in the subtropical tracers.

These observations suggest a relatively straightforward physical interpretation in terms of interactions between the meridional overturning circulation and transport along isentropic surfaces (see Fig. 2a and c). In general, air is saturated by adiabatic cooling during ascent in the overturning circulation. Because the air in the deep Tropics remains saturated throughout its ascent, the equatorial tracer values are mostly confined to their respective subdomains; as soon as the air ascends into the next subdomain, it is saturated again, thus resetting the tracers in the other subdomains.

The air that is last saturated in the upper levels then descends, largely by mixing along isentropic surfaces (Yang and Pierrehumbert, 1995). There is also, of course, a component of cross-isentropic descent associated with diabatic cooling in the descending branch of the circulation, but an overlay of the tracer fields with a plot of potential temperature (not shown) shows that the descending plumes of upper-level subtropical tracers lie almost exactly along isentropic surfaces. In this model, apparently, the diabatic descent (balanced by the Newtonian radiative cooling) of dry air directly from the top of the tropical ascent region is weak compared to the isentropic transport of dry air. The plume structures indicate that much of the air in the subtropics was last saturated in the middle and upper troposphere of the higher subtropical or lower extratropical latitudes, roughly in the subtropical jet regions. Virtually no subtropical air is saturated in the lower levels, as indicated by the very small

values of the tracers in that region.

The probability distribution for two reference locations (Fig. 4) further illustrates this point. These distributions show that the location of last saturation for the reference locations (marked by the black dots), both of which are at subtropical latitudes and a sigma level corresponding to approximately 735 hPa, were primarily in higher latitude, higher elevation subdomains, consistent with descent along isentropic surfaces. Vertical, cross-isentropic transport does make some contribution, but only a small one.

The \log_{10} of the source tracer is shown in Fig. 6e. The source tracer makes a notable contribution to the subtropical mid-troposphere. This shows that there is some upward mixing of moist air from the planetary boundary layer into those subtropical midlevels, which, having last been saturated at very high levels where the temperature is very low, would otherwise be even drier than it is. This is illustrated below in Figs. 5b, c.

The tracers can be used to produce diagnostics that summarize some aspects of the dynamical picture just described. Figure 5a shows the average temperature of last saturation (T_s). This is computed by multiplying the tracers with the temperature field rather than the saturation mixing ratio, i.e., computing the RHS of (10) with temperature replacing mixing ratio, omitting the source term, and normalizing by the sum of the contributing tracers:

$$T_s(\phi, p) = \frac{\sum_i \hat{\mathcal{T}}_i(\phi, p) T_i(\phi, p) + \sum_i \check{\mathcal{T}}_i(\phi, p) \langle T_i \rangle}{\sum_i \mathcal{T}_i} \quad (11)$$

Note the band of low T_s in the Tropics and subtropics (adjacent to the equatorial zone of high T_s) that descends to 900 mbar. These temperatures correspond to the temperature near the top of the troposphere. The temperature at the outflow region of the Hadley circulation sets the specific humidity for the dry regions of the Tropics and subtropics.

Figure 5b shows the warming experienced since last saturation ($T - T_s$). The driest regions of the Tropics and subtropics have warmed by 40 degrees or more since last saturation; this warming, coupled with the cold saturation temperature, is responsible for the extremely low relative humidities in these regions. These two diagnostics, T_s and $T - T_s$, convey information about how specific and relative humidities are set.

The warming experienced since last saturation is similar to, though not exactly the same, as the dewpoint depression (T_d , Figure 5c), which is simply the cooling required for saturation. The figures show that the maximum values of $T - T_d$ are significantly smaller than those of $T - T_s$. This difference is due to a pressure effects as well as the fact that the source tracer is not accounted for in the $T - T_s$ calculation. We can estimate the pressure effect by taking advantage of the relation, which would hold in the absence of the source term,

$$\frac{e_s(T_d)}{p} = \frac{e_s(T_s)}{p_s}, \quad (12)$$

where p is pressure and p_s is the pressure of last saturation, computed analogously to T_s . Hence we have

$$e_s(T_d) = e_s(T_s) \frac{p}{p_s} \quad (13)$$

which, after inversion of the Clausius-Clapeyron relation, yields an estimate of T_d which excludes the effect of the source term. This estimate of T_d is shown in Figure 5d. This field looks more similar to T_s than it does to T_d ; the maximum difference (not shown) between

T_s and the no-source T_d is about $8K$, whereas the maximum difference between T_s and the true T_d is over $20K$. [This is true despite the fact that the factor p/p_s (not shown) has a maximum value of about 2, because of the form of the Clausius-Clapeyron relation. At low temperatures, de_s/dT is small in absolute terms compared to its value at higher temperatures. Nonetheless it implies large *percentagewise* increases in e_s for relatively small temperature changes. Thus, while a factor of 2 in p/p_s leads to a factor of 2 difference between $e_s(T_d)$ and $e_s(T_s)$ in (13), after inverting the Clausius-Clapeyron relation this results in a relatively modest difference, less than $10K$, between T_s and T_d .] Thus while the pressure effect does contribute significantly to the reduction in the dewpoint depression relative to $T - T_s$ in the lower subtropical troposphere, the larger effect is the moistening by mixing in of humid air from below which has not been saturated since last contact with the surface.

3.3 Reconstruction of moisture fields using tracers

We now use the tracers to reconstruct the moisture fields using (10). Figs. 6a and 7a show the mixing ratio and RH fields calculated in the full model, and Figs. 6b and 7b show the fields reconstructed from the tracers. 7c shows the reconstructed RH field, as in 7b, but after application of a smoother which weights the point in question by 0.5 and each vertical and horizontal neighbor by 0.125. The reconstructed RH fields are generally close to, though slight overestimates of, the original simulated RH. The errors are partially due to the assumption of purely local saturation for the local tracer component, the assumption of a subdomain-mean saturation mixing ratio for the nonlocal components, and the zonal and time averaging of all fields.

In addition to large-scale biases, there is an obvious granularity in the unsmoothed RH

field, in which the boxes used to define the tracers are apparent. This results primarily from the different treatment of the local and nonlocal tracers. Fig. 8 shows the sum of all tracer fields, broken into local (a), nonlocal (b) and all tracers (c). The sum of all tracers is close to 1 over most of the domain, as expected, with reduced values near the surface due to the source term, and primarily at upper levels in the subtropics due to our omission of tracers in the uppermost troposphere and stratosphere. There is also a very weak granularity, which we believe to be due to numerical advection errors associated with the very strong and nonlinear tracer gradients at the box edges (see Fig. 3). The sums of the local and nonlocal tracers (Fig. 8a,b), on the other hand, have much stronger granularities. We do not understand these granular structures in great detail, but simply observe that they largely cancel when the local and nonlocal tracers are added together, yielding the much more nearly smooth structure in Fig. 8c. When the tracer fields are used to reconstruct the water vapor field, however, the different treatments of the local and nonlocal tracers lead to the persistence of the granularity in the reconstruction, as the local tracers are multiplied by the local r^* , which is smooth, while the nonlocal tracers are multiplied by the averages $\langle r^* \rangle$, which is not smooth. Using the latter for both tracers might be more consistent, but yields a result which is less accurate overall. If we could afford to reduce the box size to the model grid size, we expect the granularity in all fields would vanish.

It is instructive to separately plot the three components of the moisture fields as reconstructed from (10): local, nonlocal, and source tracer components. Figs. 6c-e and 7d-f show how these components contribute to the mixing ratio (plotted logarithmically) and RH.

As expected, the local tracer component is the primary source of mixing ratio in the deep tropics and contributes relatively little to the arid region of the subtropics. The nonlocal tracer component, in contrast, contributes much of the mixing ratio in the arid zone. The

source tracer, not surprisingly, is responsible for much of the mixing ratio in the lowest levels.

The RH fields show a slightly different picture. The local effects are primarily responsible for the RH in the deep tropics and the upper troposphere of the extratropics, while the nonlocal effects contribute positively to the RH in the lower troposphere of the extratropics. Of course, a tracer can also be important by keeping the air dry, i.e., importing a low value of T_s . In this sense, nonlocal effects are important to the RH of the subtropics, though they contribute almost zero in Fig. 7d. The source term provides an important contribution to the lower levels in the tropics and subtropics.

3.4 Application to Comprehensive GCMs

The technique presented here can potentially be used in comprehensive GCMs to understand the large-scale controls on relative humidity. The GCM used here is highly idealized as there are no convective or microphysical parameterizations. To the extent that microphysics is important in controlling the relative humidity, our technique may also be useful as a way of demonstrating and quantifying the role of microphysics in maintaining global relative humidity. Since we have shown that, with adequate resolution, our technique can reconstruct the water vapor distribution relatively accurately, any larger differences between the reconstructed and simulated fields in a more comprehensive GCM can potentially be ascribed to cloud microphysics. Alternatively, the technique could be augmented by adding very simple models for the retention of condensate along trajectories. The simplest such approach would be simply to increase the effective r^* at saturation by some amount, representing liquid or frozen water which will evaporate as the parcel descends; the most complex might be a microphysical model comparable to that used by Gettelman et al. (2002) to study interactions

of cirrus clouds and water vapor near the tropical tropopause (presuming that the GCMs microphysical scheme were still more complex than this).

Although we have focused on the troposphere in this study, the tracer technique described here could potentially be applied to the tropopause and stratosphere by using higher model resolution in the upper levels. Water transport between the troposphere and stratosphere is controlled by a combination of rapid ascent during convection, slow diabatic ascent (Holton et al., 1995; Webster and Heymsfield, 2003), and horizontal transport through “cold traps” (Holton and Gettleman, 2001), though the precise relationship between these processes is not well understood. Because our tracer-based technique is a particularly good probe of the pathways of unsaturated air, it may be useful for investigating some of the issues related to tropopause and stratosphere relative humidity.

4 Conclusions

We have presented a technique for diagnosing the contributions of temperature and circulation to the water vapor distribution in a numerical model. We divide the atmosphere into subdomains, and define a tracer for each subdomain which represents air which was last saturated there. From the spatial distributions of these tracers and the temperature field, we can reconstruct the water vapor distribution in the model.

We have applied our method to simulations with an idealized GCM in which the dynamics are dry but the circulation carries a passive water-like tracer, whose source is at the surface and whose sink is large-scale condensation with no condensate retained and zero latent heat released to the atmosphere. In this simulation, the only errors in our technique result from spatial and temporal averaging, and it is shown that these errors are small with the resolution

we use (28 subdomains over the globe). In this particular model, the results show that the dry air in the lower subtropical troposphere is produced primarily by isentropic mixing from higher latitudes, with diabatic descent from lower latitudes making only a weak contribution.

Using this method, we can compute a number of diagnostics which illuminate the dynamics governing the water vapor distribution, such as the average temperature change since last saturation ($T - T_s$) and the probability distribution of the location of last saturation. The dew point depression is shown to be significantly smaller than $T - T_s$, partly because of the pressure effect, but more significantly because of the mixing upward of moist air which has not been saturated since last contact with the surface.

The value of the technique used here lies in its use as a diagnostic to distinguish the roles of temperature and circulation in determining the water vapor distribution. When applied to a comprehensive GCM with a full range of physical parameterizations, this diagnostic will, at a minimum, allow an assessment of the relative importance of cloud microphysics relative to circulation and temperature. If the influence of cloud microphysics were to turn out to be relatively small, the technique would allow the roles of temperature and circulation separately to be assessed.

Acknowledgments

This research was supported by the David and Lucile Packard Foundation.

References

- Colella, P. and P. Woodward, 1984: The piecewise parabolic method (PPM) for gas-dynamical simulations. *Journal of Computational Physics*, **54**, 174–201.
- Dessler, A. and S. Sherwood, 2000: Simulations of tropical upper tropospheric humidity. *Journal of Geophysical Research*, **105**(D15), 20,155–20,163.
- Ebert, E., U. Schumann and R. Stull, 1989: Nonlocal turbulent mixing in the convective boundary layer evaluated from large eddy simulation. *J. Atmos. Sci.*, **46**, 2178–2207.
- Gettelman, A., W. Randel, F. Wu and S. Massie, 2002: Transport of water vapor in the tropical tropopause layer. *Geophysical Research Letters*, **29**(1).
- Haine, T. and T. Hall, 2002: A generalized transport theory: Water-mass composition and age. *J. Phys. Oceanog.*, **32**, 1932–1946.
- Hall, T. and R. Plumb, 1994: Age as a diagnostic of stratospheric transport. *J. Geophys. Res.*, **99**, 3539–3558.
- Held, I. and M. Suarez, 1994: A proposal for the intercomparison of the dynamical cores of atmospheric general circulation models. *Bulletin of the American Meteorological Society*, **75**(10), 1825–1830.
- Holton, J. and A. Gettleman, 2001: Horizontal transport and dehydration in the stratosphere. *Geophysical Review Letters*, **28**, 2799–2802.
- Holton, J., P. Haynes, A. Douglass, R. Rood and L. Pfister, 1995: Stratosphere–troposphere exchange. *Reviews of Geophysics*, **33**, 403–439.

- Holzer, M. and T. Hall, 2000: Transit-time and tracer-age distributions in geophysical flows. *J. Atmos. Sci.*, **57**, 3539–3558.
- Larson, V., 1999: The relationship between the transilient matrix and the Green’s function for the advection-diffusion equation. *J. Atmos. Sci.*, **56**, 2447–2453.
- Lin, S.-J. and R. Rood, 1996: Multidimensional flux form semi-Lagrangian transport schemes. *Monthly Weather Review*, **124**, 2046–2070.
- Peixoto, J. and A. Oort, 1992: *Physics of Climate*. AIP Press.
- Pierrehumbert, R. and R. Roca, 1998: Evidence for control of Atlantic subtropical humidity by large scale advection. *Geophysical Research Letters*, **25**(24), 4537–4540.
- Salathe, E. P. and D. L. Hartmann, 1997: A trajectory analysis of tropical upper-tropospheric moisture and convection. *Journal of Climate*, **10**, 2533–2547.
- Sherwood, S., 1996: Maintenance of the free-tropospheric Tropical water vapor distribution. Part II: Simulation by large-scale advection. *Journal of Climate*, **9**, 2919–2934.
- Simmons, A. and D. Burridge, 1981: An Energy and Angular-Momentum Conserving Vertical Finite-Difference Scheme and Hybrid Vertical Coordinates. *Monthly Weather Review*, **109**(4), 758–766.
- Sobel, A., 1999: Diffusion vs. nonlocal models of stratospheric mixing, in theory and practice. *J. Atmos. Sci.*, **56**, 2571–2584.
- Stull, R., 1984: Transilient turbulence theory. Part I: The concept of eddy-mixing across finite distances. *J. Atmos. Sci.*, **41**, 3351–3367.

- Stull, R., 1993: Review of non-local mixing in turbulent atmospheres: Transilient turbulence theory. *Boundary Layer Meteor.*, **62**, 21–96.
- van Leer, B., 1979: Toward the ultimate conservative difference schemes. V: A second order sequel to Godunov method. *Journal of Computational Physics*, **32**, 101–136.
- Webster, C. and A. Heymsfield, 2003: Water Isotope Ratios D/H, $^{18}\text{O}/^{16}\text{O}$, $^{17}\text{O}/^{16}\text{O}$ in and out of Clouds Map Dehydration Pathways. *Science*, **302**(5651), 1742–1745.
- Yang, H. and R. Pierrehumbert, 1995: Production of dry air by isentropic mixing. *J. Atmos. Sci.*, **51**, 3437–3454.

List of Figures

1	Example tracer field illustrating how tracers are divided into local and nonlocal components	25
2	Zonal-mean fields calculated from FMS with large-scale moisture advection and condensation. (a) Relative humidity; (b) $\log_{10}(r)$ (c) Streamfunction. Negative values are dashed; (d) Potential Temperature (K)	26
3	The time-mean, zonal-mean of the 28 tracers used in this calculation. Horizontal axes are latitude (degrees); vertical axes are pressure (hPa)	27
4	The smoothed probability distribution for location of last saturation for two reference points (marked by red dot). Only the southern hemisphere is shown.	28
5	(a) Contour plot of T_s , the temperature of last saturation; (b) $(T - T_s)$, the amount of warming each parcel of air has experience since last saturation; (c) dewpoint depression; (d) dewpoint depression due to pressure effects	29
6	(a) Mixing ratio calculated from the full model; (b) mixing ratio reconstructed from tracers; (c) mixing ratio due to local tracer component; (d) mixing ratio due to nonlocal tracer component; (e) mixing ratio due to source tracer. All quantities are presented as the \log_{10} of the value.	30
7	(a) Relative humidity calculated from the full model; (b) relative humidity reconstructed from tracers; (c) smoothed reconstructed relative humidity; (d) relative humidity due to local tracer component; (e) relative humidity due to nonlocal tracer component; (f) relative humidity due to source tracer	31
8	Relationship of (a) local, (b) nonlocal, and (c) sum of all tracer components.	32

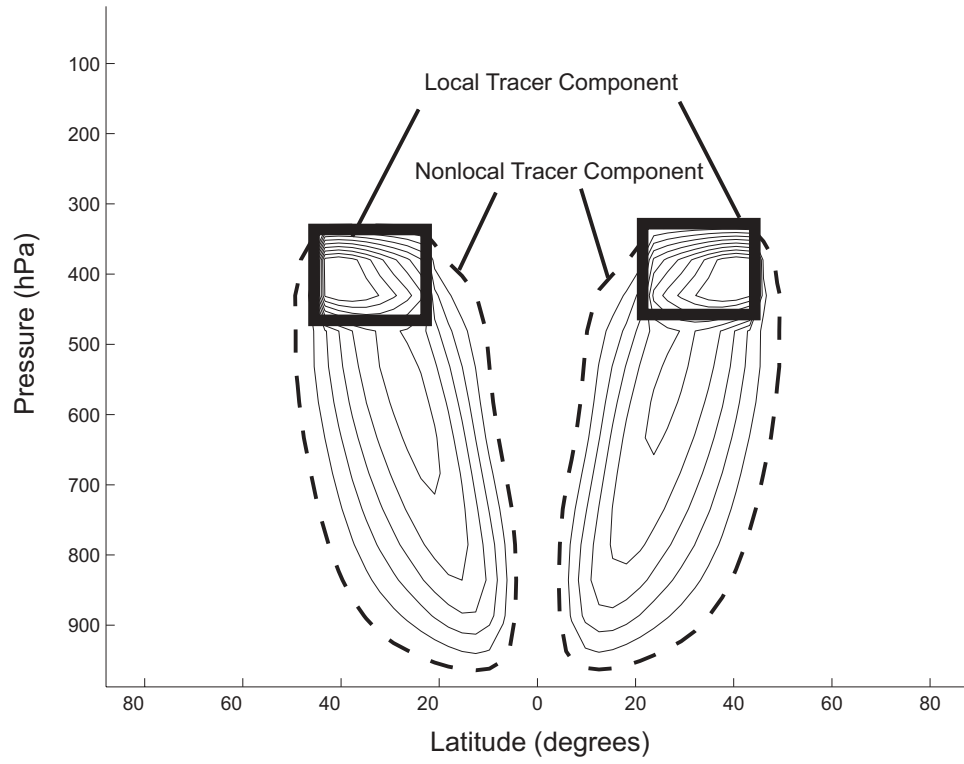


Figure 1: Example tracer field illustrating how tracers are divided into local and nonlocal components

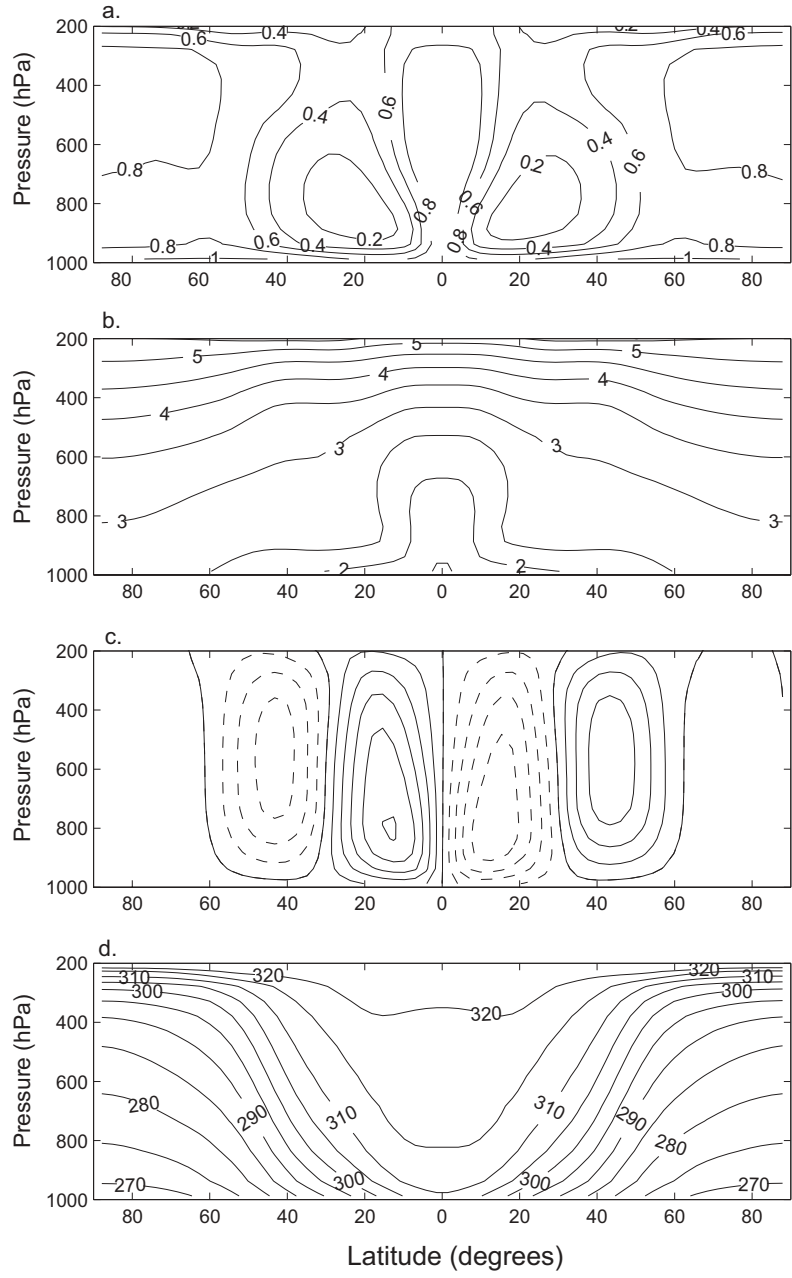


Figure 2: Zonal-mean fields calculated from FMS with large-scale moisture advection and condensation. (a) Relative humidity; (b) $\log_{10}(r)$ (c) Streamfunction. Negative values are dashed; (d) Potential Temperature (K)

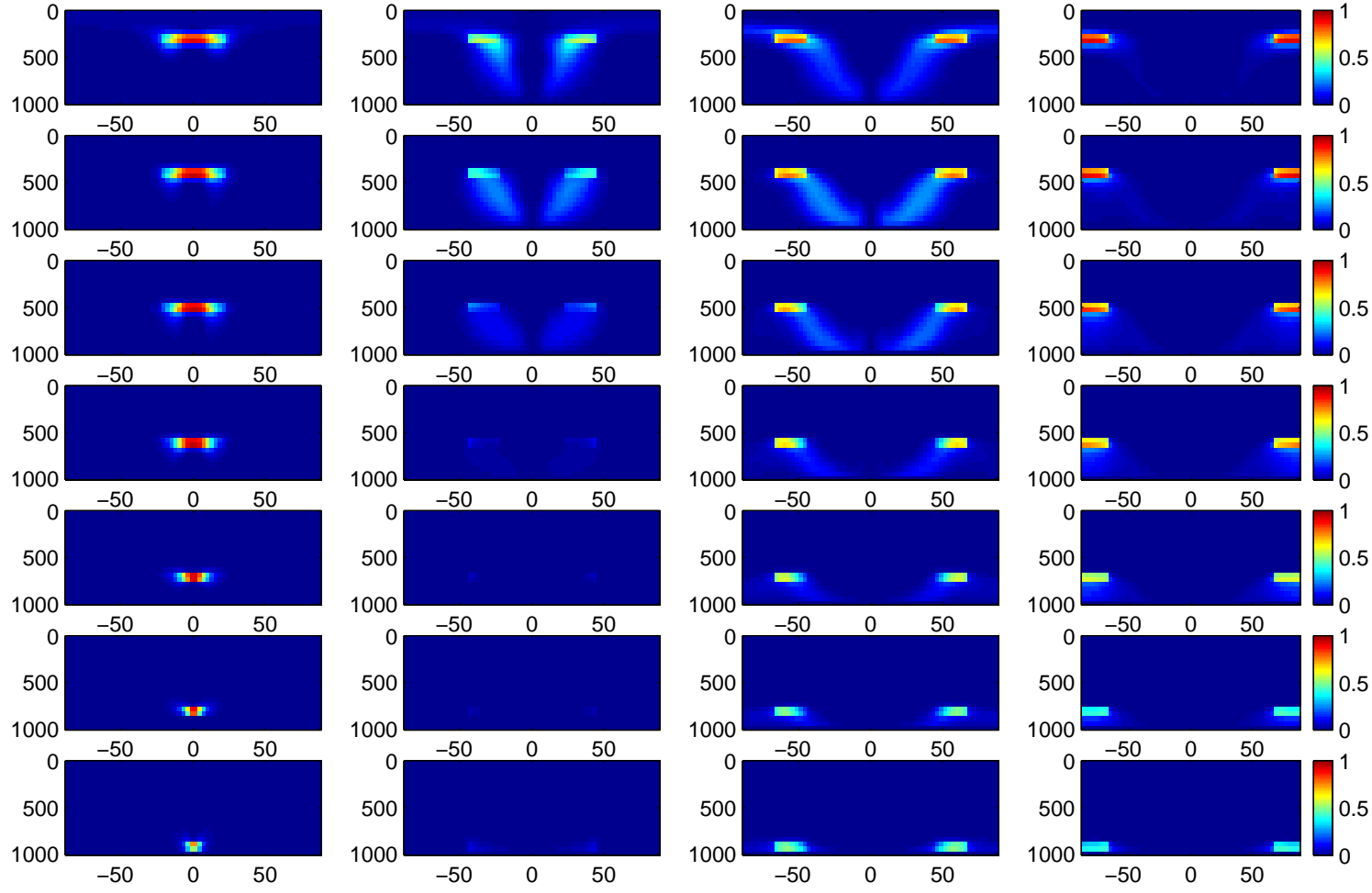


Figure 3: The time-mean, zonal-mean of the 28 tracers used in this calculation. Horizontal axes are latitude (degrees); vertical axes are pressure (hPa)

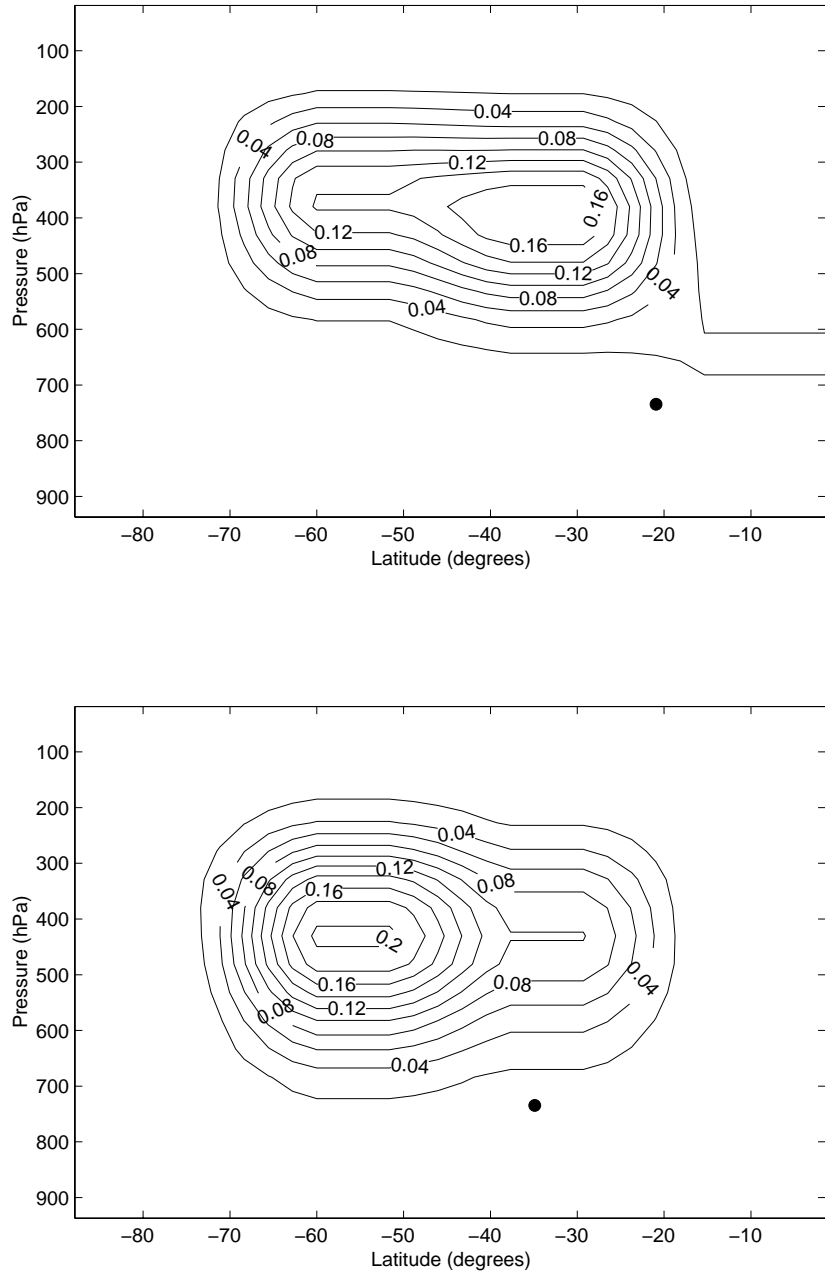


Figure 4: The smoothed probability distribution for location of last saturation for two reference points (marked by red dot). Only the southern hemisphere is shown.

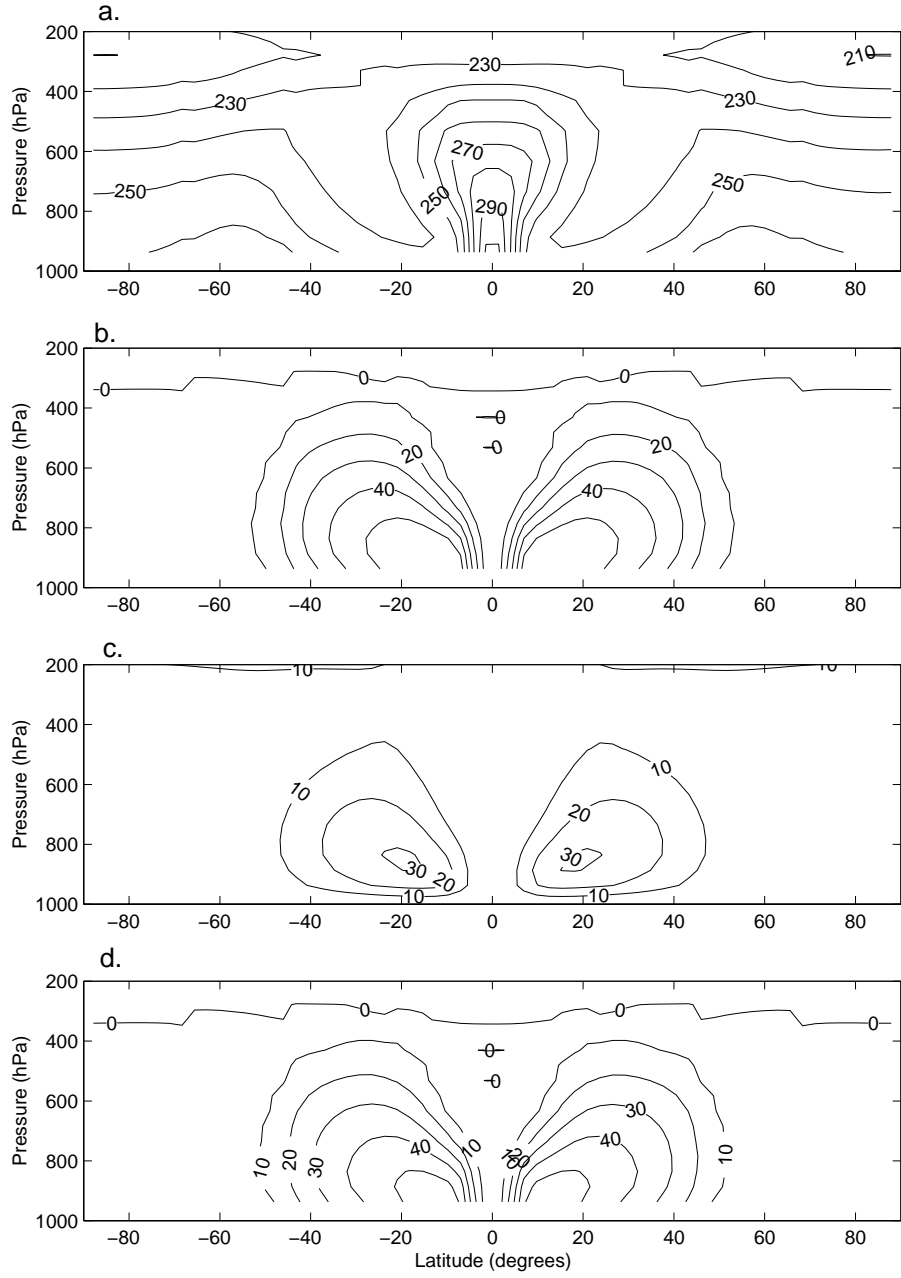


Figure 5: (a) Contour plot of T_s , the temperature of last saturation; (b) $(T - T_s)$, the amount of warming each parcel of air has experience since last saturation; (c) dewpoint depression; (d) dewpoint depression due to pressure effects

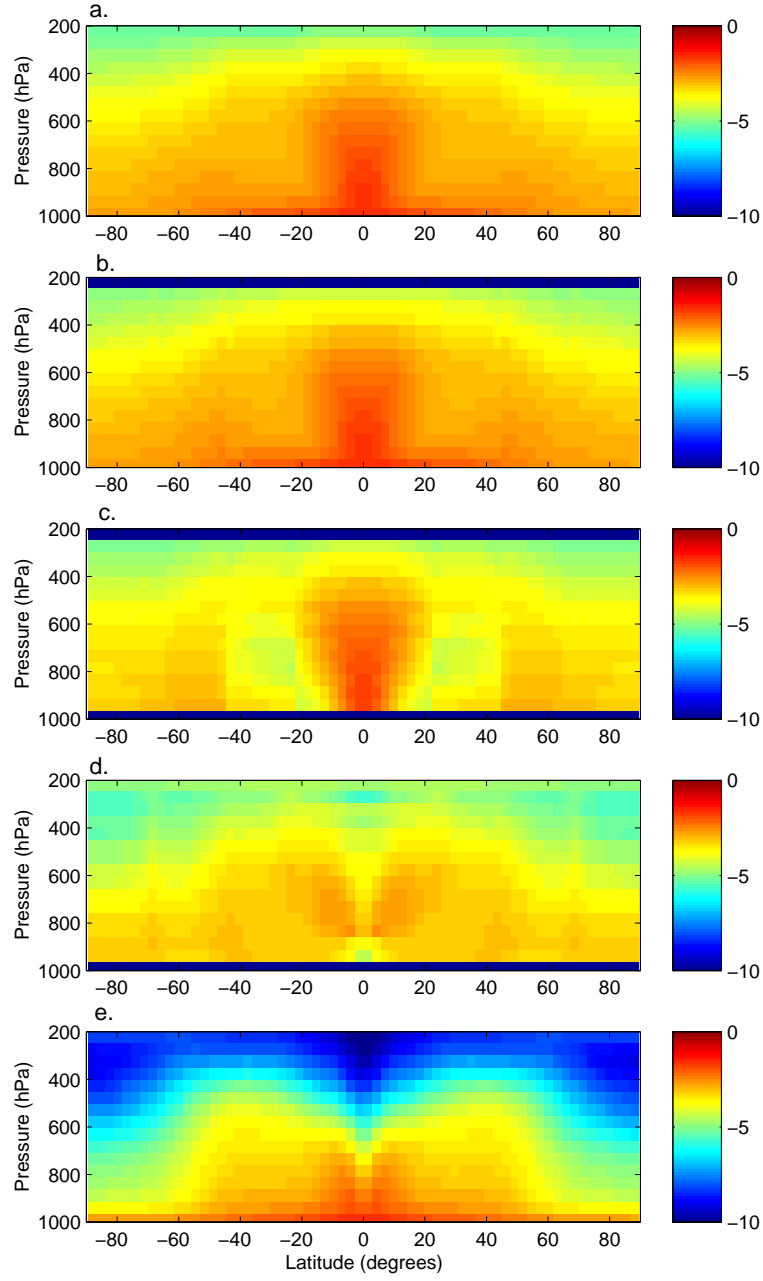


Figure 6: (a) Mixing ratio calculated from the full model; (b) mixing ratio reconstructed from tracers; (c) mixing ratio due to local tracer component; (d) mixing ratio due to nonlocal tracer component; (e) mixing ratio due to source tracer. All quantities are presented as the \log_{10} of the value.

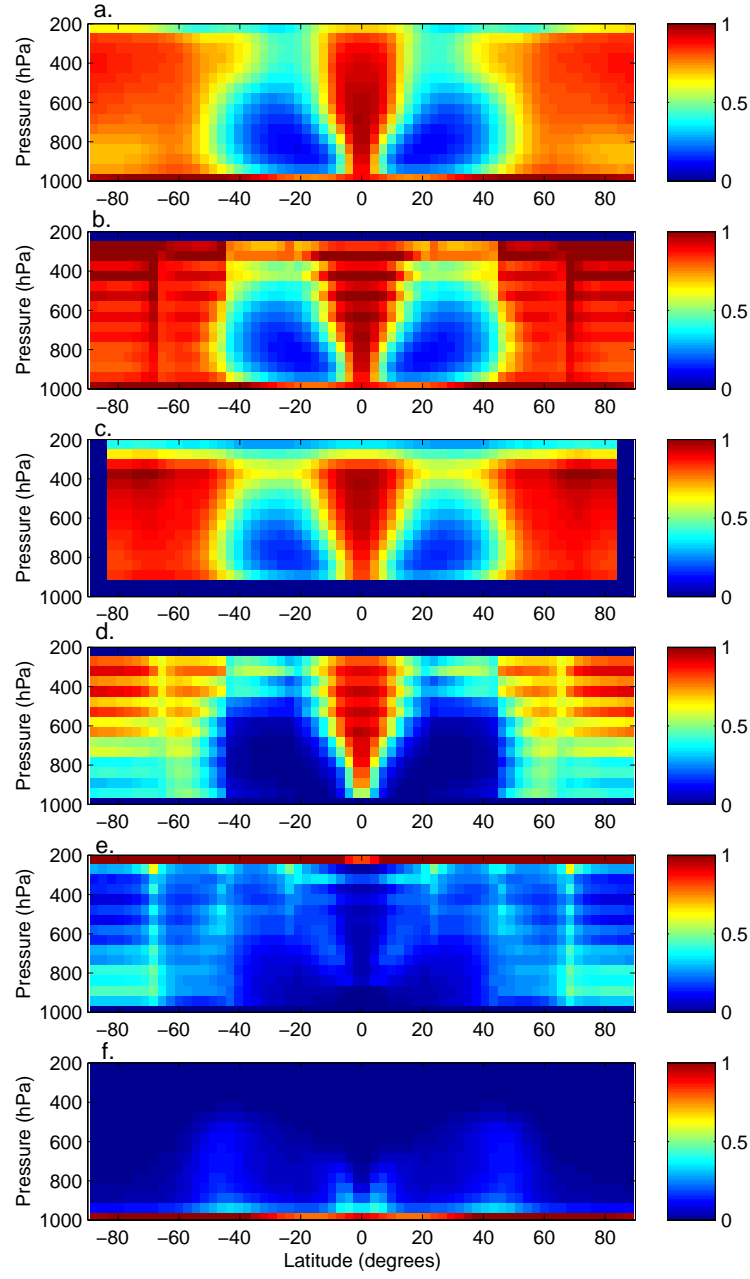


Figure 7: (a) Relative humidity calculated from the full model; (b) relative humidity reconstructed from tracers; (c) smoothed reconstructed relative humidity; (d) relative humidity due to local tracer component; (e) relative humidity due to nonlocal tracer component; (f) relative humidity due to source tracer

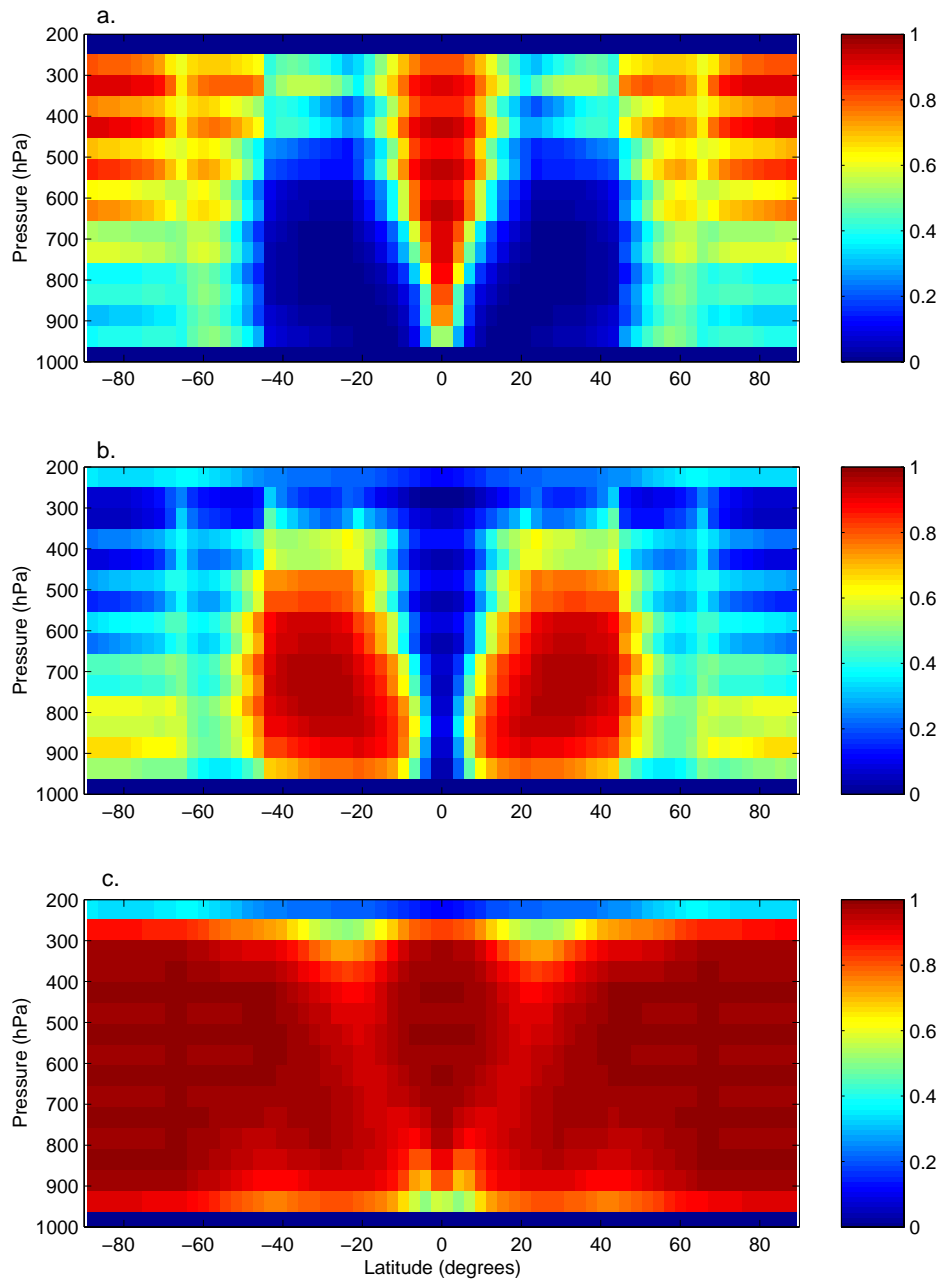


Figure 8: Relationship of (a) local, (b) nonlocal, and (c) sum of all tracer components.